

Performing a stellar autopsy using the radio-bright remnant of SN 1996cr

C. Meunier^{1*}, F. E. Bauer^{1,2,3†}, V. V. Dwarkadas^{4‡}, B. Koribalski⁵, B. Emonts⁵, R. W. Hunstead⁶, D. Campbell-Wilson⁶, C. Stockdale⁷, S. J. Tingay⁸

¹*Pontificia Universidad Católica de Chile, Departamento de Astronomía y Astrofísica, Casilla 306, Santiago 22, Chile*

²*Space Science Institute, 4750 Walnut Street, Suite 205, Boulder, Colorado 80301*

³*Columbia Astrophysics Laboratory, 550 W. 120th St., Columbia University, New York, NY 10027*

⁴*Department of Astronomy and Astrophysics, U Chicago, 5640 S Ellis Ave, Chicago, IL 60637*

⁵*Australia Telescope National Facility, CSIRO Astronomy and Space Science, PO Box 76, Epping, NSW, 1710, Australia*

⁶*Sydney Institute for Astronomy, School of Physics, University of Sydney, NSW 2006, Australia*

⁷*Department of Physics, Marquette University, P.O. Box 1881, Milwaukee, WI 53201-1881, USA*

⁸*International Centre for Radio Astronomy Research, Curtin University, Bentley 6102, WA, Australia*

ABSTRACT

We present newly reduced archival radio observations of SN 1996cr in the Circinus Galaxy from the Australia Telescope Compact Array (ATCA) and the Molonglo Observatory Synthesis Telescope (MOST), and attempt to model its radio light curves using recent hydrodynamical simulations of the interaction between the SN ejecta and the circumstellar material (CSM) at X-ray wavelengths. The radio data within the first 1000 days show clear signs of free-free absorption (FFA), which decreases gradually and is minimal above 1.4 GHz after day ~ 3000 . Constraints on the FFA optical depth provide estimates of the CSM free electron density, which allows insight into the ionisation of SN 1996cr’s CSM and offers a test on the density distribution adopted by the hydrodynamical simulation. The intrinsic spectral index of the radiation shows evidence for spectral flattening, which is characterised by $\alpha = 0.852 \pm 0.002$ at day 3000 and a decay rate of $\Delta\alpha = -0.014 \pm 0.001 \text{ yr}^{-1}$. The striking similarity in the spectral flattening of SN 1987A, SN 1993J, and SN 1996cr suggests this may be a relatively common feature of SNe/CSM shocks. We adopt this spectral index variation to model the synchrotron radio emission of the shock, and consider several scalings that relate the parameters of the hydrodynamical simulation to the magnetic field and electron distribution. The simulated light curves match the large-scale features of the observed light curves, but fail to match certain tightly constraining sections. This suggests that simple energy density scalings may not be able to account for the complexities of the true physical processes at work, or alternatively, that the parameters of the simulation require modification in order to accurately represent the surroundings of SN 1996cr.

Key words: supernovae: individual: SN 1996cr; supernovae: general; circumstellar matter; stars: winds; methods: numerical

1 INTRODUCTION

Radio and X-ray emission arising from remnants of supernovae (SNe) provide rich information about the ongoing interaction between the SN ejecta and the circumstellar material (CSM). The fact that SN ejecta expand ~ 2 – 3 orders

of magnitude faster than the slower-moving progenitor stellar wind ensures that, in a matter of decades, the ejecta will have swept up and revealed information on tens to thousands of years of stellar evolution leading up to the explosion, thus providing an alternate window for studying the evolution and classification of the progenitor stars (Chevalier & Fransson 1994).

An analytical model of the emission from radio SNe (RSNe) was developed by Chevalier (1982, hereafter the ‘standard’ model), in which the SN ejecta and CSM den-

* E-mail: clmeunie@uc.cl

† fbauer@astro.puc.cl

‡ vikram@oddjob.uchicago.edu

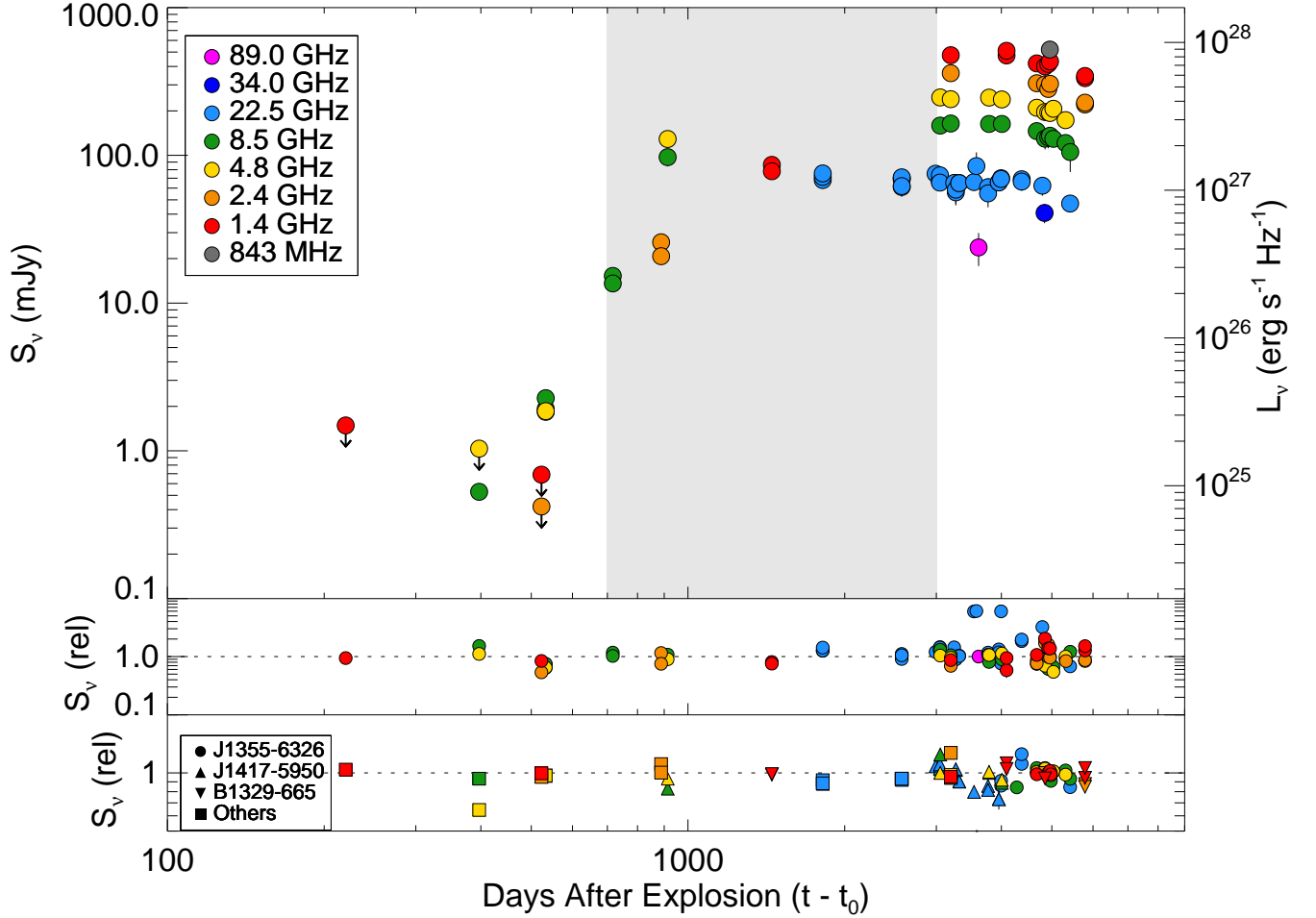


Figure 1. Observed radio flux densities (filled circles) for SN 1996cr along with 1σ error bars (which are smaller than symbols in some cases); when no secure detection is obtained we show 3σ upper limits (e.g., at early times). The gray-shaded region denotes the period between days ~ 700 – 3000 when the shock is believed to be travelling through the dense shell. Three regions are clearly defined, with low early emission (for which only upper limits are available), a flux rise at ~ 700 d when the shock begins to interact with the shell, and a late-time plateau region with a possible turnover at day ~ 5000 . Also shown are the relative flux densities for the host AGN nucleus (middle panel) and various phase flux calibrators (lower panel). The nucleus values were normalised based on the average values at each frequency found in the highest resolution configurations only (e.g., 6A), while the calibrators were normalised based on their historical values at each frequency. In general, the nucleus only varies by ≈ 10 – 30% , while the calibrators vary by ≈ 10 – 20% . These should provide strict empirical upper limits to any uncertainties on SN 1996cr’s variability.

sity profiles are described as power laws in radius, and the evolution of the shock front is characterised by a self-similar solution in which the shock radii expand as power laws in time. The interaction between the SN ejecta and the CSM leads to the formation of a contact discontinuity, bounded by a forward shock travelling into the CSM and a reverse shock moving back into the ejecta relative to the contact discontinuity. The radio emission arising from these two shocks is typically characterised as synchrotron radiation from ultrarelativistic electrons accelerated at the shock front (Duffy et al. 1995; Reynolds 2008). If the energy density of the magnetic field as well as the relativistic particles can be assumed as proportional to the thermal energy density, then this treatment provides a simple formula for the radio emission. This has been successful in describing the radio light curves of SNe exploding into simple red supergiant (RSG)

type winds, where the emission decreases as a power-law in time (Weiler et al. 2002). It fails, however, to account for the light curves of RSNe which do not decrease in power-law fashion, and therefore where the CSM has presumably been altered by perhaps a binary companion, or by various evolutionary stages both on or after the main sequence (cf. table 4 in Soderberg et al. 2006).

The late-stage evolution of stars more massive than $\sim 20M_{\odot}$ should extend beyond the initial post-main sequence RSG phase into yellow or blue supergiant (YSG, BSG), luminous blue variable (LBV), and/or Wolf-Rayet (WR) phases (e.g., Lamers et al. 1991; Stothers & Chin 1996). The relatively high mass-loss rates and/or wind velocities often present during these later phases (e.g., Nugis & Lamers 2000; Vink et al. 2011) can result in stellar winds with enough momentum to sweep up ambient

material deposited by winds during previous evolutionary stages of the star, creating a low-density cavity bordered by a dense shell of swept-up material (Weaver et al. 1977). Once the progenitor explodes, the ejecta expand within this complex CSM, which is not represented by a power-law density profile, and for which the standard model, which assumes self-similar shock expansion, is not applicable (Chevalier & Liang 1989; Tenorio-Tagle et al. 1990, 1991; Dwarkadas 2005; Dwarkadas 2007a). We *must* therefore model the ejecta-CSM interaction through hydrodynamical simulations using prescribed ejecta and CSM density profiles. The resulting hydrodynamical quantities (pressure, density and temperature) can then be input to radiative transfer equations to simulate the radio light curves and spectra of the SN (e.g., Martí-Vidal et al. 2011; Mioduszewski et al. 2001).

We employ a simplified version of this method to study the radio light curve of SN 1996cr, located in the Circinus Galaxy (~ 3.8 Mpc; Freeman et al. 1977; Koribalski et al. 2004), which exploded around 1996 and was confirmed as a type II_n SN by Bauer et al. (2007) ~ 11 yr later. Serendipitous archival data provide a crude picture of the explosion dynamics and the late evolutionary history of the progenitor (see, e.g., Bauer et al. 2008 and references therein). In behaviour reminiscent of SN 1987A (Park et al. 2005; Zanardo et al. 2010), SN 1996cr shows an increase of X-ray and radio luminosity in the years following the initial explosion. Dwarkadas et al. (2010) studied SN 1996cr through hydrodynamic simulations of the ejecta-CSM interaction, from which they accurately reproduced the X-ray light curves and spectra, and in doing so derived valuable constraints on the CSM distribution: SN 1996cr exploded in a low-density medium and expanded freely before interacting with a dense shell of material at about 0.04 pc, which is thought to be the result of the interaction between fast winds of either a BSG or WR star and a slower wind, possibly from a previous RSG stage which is not yet well constrained by observations.

In this work we provide an observational update on the radio evolution of SN 1996cr, and attempt to compute the radio light curves from the hydrodynamic simulation in Dwarkadas et al. (2010). The constraints on the simulation parameters came primarily from the observed X-ray light curves and spectra. However, there are no X-ray detections prior to year 2000, and only a few relatively weak soft X-ray upper limits before that (Bauer et al. 2008; Dwarkadas et al. 2010). Thus for the epoch when the shock is thought to have first encountered the dense shell in 1997, there are no direct thermal constraints on the density of the inner cavity implemented in the simulation. Radio detections of SN 1996cr start as early as mid-1996, and could provide constraints on the CSM density during this period, since both the X-ray and radio emissions can be ultimately related to the density of the emitting region. Probing the CSM density of the inner boundary of the shell and possibly even the initial cavity using the radio light curve may ultimately help to refine some of the uncertainties in the hydrodynamic simulation, give us a better picture of the CSM structure, and thereby provide more information about the progenitor star and its evolution.

This study is organised as follows. Radio data and reduction methods are detailed in §2. In §3 we characterise the observational properties of SN 1996cr, and outline how

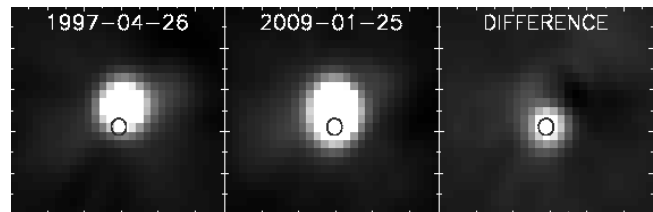


Figure 2. We show two 843 MHz images from MOST for the central $4''.5 \times 4''.5$ of the Circinus Galaxy before (left panel) and after (middle panel) SN 1996cr became visible at 843 MHz, as well as a difference image with the clear SN 1996cr detection (right panel). A $10''$ radius black circle denotes the position of SN 1996cr in all panels for reference. All of the images are scaled linearly on an identical stretch from $S_\nu = 0.05$ –1 Jy. The sidelobes in the images come from the central gap in the array and do not fully subtract out due to radio interference.

we translate the hydrodynamic simulation into a radio emission model. In §4 we explore the HII region surrounding SN 1996cr and present the simulated radio light curves. Finally, in §5 we discuss the results and implications of this study. In this paper, we adopt the explosion epoch of 1995.6 determined in Bauer et al. (2008). All errors are quoted at 1σ unless otherwise stated.

2 RADIO OBSERVATIONS

Bauer et al. (2008) provide radio data up to 2007. However, since more data exist for comparison, and some of the data presented in Bauer et al. (2008) were re-reduced to clean up artifacts and incorporate a larger array of calibration data, we detail the data reduction procedures here. The data presented here supersede those of Bauer et al. (2008).

Numerous observations of the Circinus Galaxy exist from studies at radio wavelengths spanning 1995 to 2011 (e.g., Elmouttie et al. 1995; Greenhill et al. 1997; Jones et al. 1999; McCallum et al. 2005, 2009; Phillips et al. 1998; Wilson et al. 2011). These were retrieved from the Australia Telescope Compact Array (ATCA) archive¹ and were reduced with MIRIAD (v4.0.5 and v20110616) following the procedures outlined in the ATNF Miriad User Manual². Fluxes for SN 1996cr are presented in Table 1 and Fig. 1.

For the 1.4, 2.4, 4.8, and 8.5 GHz observations, the ‘primary’ flux calibrator was typically PKS B1934–638, with approximate flux densities of 14.9, 11.6, 5.8, and 2.8 Jy, respectively. For 15–25 GHz observations the ‘primary’ flux calibrators were either PKS B1934–638 (0.7–1.2 Jy) or PKS B1921–293 (10–25 Jy). For the 36 GHz and 89 GHz observations, the primary calibrators were Mars and Uranus.

The secondary calibrators, which served as the gain, bandpass, and phase calibrators for the Circinus Galaxy, varied from observation to observation and were variable in time, and include (in descending order of use) sources PKS B1921–293 (bandpass, alternate 22.5 GHz flux), PKS B0823–500 (bandpass, alternate flux), PMN J1355–6326 (phase), PMN J1417–5950 (phase), PKS B1329–665 (bandpass, phase), PKS B1718–649 (phase), PKS B1549–790

¹ <http://atoa.atnf.csiro.au/>

² <http://www.atnf.csiro.au/computing/software/miriad/>

(phase), PMN J1047–6217 (phase), PKS B1104–445 (phase), PKS B1424–418 (phase), PKS B1610–771 (phase), PMN J1342–5828 (phase) and PKS B1236–684 (phase). Flux densities for the calibrators are provided in the Appendix. To cross-check our flux calibration, the flux densities of the secondary calibrators were compared to their average or interpolated historical values from calibration monitoring efforts³. Importantly, aside from one case at day ~ 400 , and in spite of sometimes strong intrinsic variability and scintillation effects, the phase calibrators never strayed more than $\approx 20\%$ from their nominal historical values, as shown in Fig. 1. Both source and calibration data were inspected with the aim to flag and remove bad time intervals and channels, time intervals strongly affected by interference, and obvious emission and absorption lines. The calibration tables were applied to the Circinus Galaxy data, from which deconvolved, primary-beam-corrected images were made. Due to the increasing beam size of ATCA with decreasing frequency, we measured flux densities using only the 6 km baselines for frequencies below 4 GHz in order to limit contamination to SN 1996cr from the diffuse emission of the host galaxy. Phase self-calibration was employed when feasible, and only if it led to a substantial improvement in the rms noise. Point-source flux densities (determined from IMFIT or UVFIT) or 3σ upper limits (determined from IMSTAT) were then determined for SN 1996cr. These values are provided in Table 1 and shown in Fig. 1. The larger errors on the 15–90 GHz data points reflect greater uncertainties in atmospheric corrections and flux calibrators. Some of the dispersion among the 15–25 GHz points could also arise from contamination by weak H₂O maser emission that was not flagged from the continuum (e.g., Greenhill et al. 1997; McCallum et al. 2007).

The only other strong point source in the field of view is the nucleus of the Circinus Galaxy, which is primarily due to emission from the Compton-thick AGN as well as a compact circumnuclear starburst. Flux measurements from the point-like nucleus were extracted in a manner identical to SN 1996cr. These are shown in Fig. 1 and provided in the Appendix. While the nucleus could vary intrinsically and can additionally be contaminated at long wavelengths by diffuse emission from the extended disk, it at least provides us with a secondary estimate of any systematic error associated with each observation. We find that the majority of measurements of the nucleus lie between 10–30% of its mean total flux in each band, although some observations vary upwards considerably. For instance, at 22.5 GHz there may be possible contamination from water maser emission and varies by a factor of up to four, while at low frequencies the host galaxy contaminates as a function of the beamsize and varies by factors as large as ~ 10 –50. Thus aside from our previously stated reservations regarding the 15–90 GHz data, we are generally confident in our calibrated fluxes for SN 1996cr.

SN 1996cr was observed on 2009 January 25 with the Molonglo Observatory Synthesis Telescope (MOST) at 843 MHz with a synthesised beam of $47'' \times 43''$ at a position angle of 0° . The MOST data were reduced and calibrated using a custom process described in Bock et al. (1999). Given the $24''$ north-south separation of SN 1996cr from the bright nu-

cleus of the Circinus Galaxy, the supernova emission was completely blended with that of the galaxy. Fortunately, there were three prior MOST observations of this field with SN 1996cr absent or self-absorbed: 1989 April, 1996 April and 1997 April. Difference images were formed after regridding all images to a common reference frame (see Fig. 2). A point source fit to each difference image yielded a mean flux density for SN 1996cr of 520 ± 30 mJy and a position fully consistent with the Chandra position. Note that the total flux density for the Circinus Galaxy in 1996 was $\sim 2.15 \pm 0.15$ Jy at 843 MHz. Since the flux contribution from the AGN is expected to be minimal (roughly 75 mJy with only 10–30% variability), the observed flux must arise almost exclusively from diffuse component and hence should not vary.

3 MODELLING THE LIGHT CURVE

3.1 Radio Emission

The interaction between the SN ejecta and the CSM results in the formation of a double-shocked structure separated by a contact discontinuity. Charged particles are accelerated to relativistic energies across the shock front, giving rise to non-thermal synchrotron emission in the presence of a strong magnetic field. Electrons, being substantially less massive, are easier to accelerate (in the direction perpendicular to their motion) by the magnetic field, and end up dominating the emission. Their energy distribution is assumed to be a power law of the form $N(E) = K E^{-\gamma}$, where E is the electron energy, K is the normalisation of the distribution, and γ is the electron spectral index. Following the prescription given in Chevalier (1982), the synchrotron luminosity L_ν at frequency ν is:

$$L_\nu = 4\pi R^2 \Delta R K B^{\alpha+1} \nu^{-\alpha} e^{-\tau} \text{ (erg s}^{-1}\text{Hz}^{-1}\text{)}, \quad (1)$$

where ΔR is the thickness of the synchrotron-emitting region at radius R , assumed in this case to be the spherically symmetric region encompassing the forward and reverse shocks, B is the magnetic field strength, the radio spectral index is $\alpha = (\gamma - 1)/2$, and τ is the optical depth.

Radio emission can be absorbed either by synchrotron self-absorption (SSA) or free-free absorption (FFA) from CSM both inside (attenuating backside emission) and outside (attenuating all emission) of the forward shock, leading to telltale low-frequency absorption. We initially assume all of the absorption is due to FFA (see Sec. 3.2 for reasoning) and use the form of the FFA optical depth given in Altenhoff et al. (1960):

$$\tau_{\text{ff}} = 8.235 \times 10^{-2} \nu_{\text{GHz}}^{-2.1} \int_0^{s_{\text{pc}}} N_e^2 \text{cm}^{-3} T_K^{-1.35} ds_{\text{pc}}, \quad (2)$$

where T is the temperature of the CSM, ν is the frequency and N_e is the line-of-sight electron number density. Early absorption can be high due to the strong density gradient in the stellar wind, which should decrease as the shock wave overtakes more of the CSM, resulting in a rapid frequency-dependent turn-on like that observed in the spectra of SN 1996cr in Fig. 3.

³ <http://www.narrabri.atnf.csiro.au/calibrators/>

Table 1. ATCA Radio Observations

Obs. Date	Days from explosion	Obs. ID	Array	W-Band		K _A -Band		K-Band		X-Band		C-Band		S-Band		L-Band		UHF	
(1)	(2)	(3)	(4)	ν (5)	S_ν (6)	ν (7)	S_ν (8)	ν (9)	S_ν (10)	ν (11)	S_ν (12)	ν (13)	S_ν (14)	ν (15)	S_ν (16)	ν (17)	S_ν (18)	(19)	(20)
1995-03-03	-120	C204a	750A	—	—	—	—	—	—	8640	< 0.3	4800	< 0.6	—	—	—	—	—	—
1995-03-03	-120	C204a	750A	—	—	—	—	—	—	8640	< 0.3	4800	< 0.4	—	—	—	—	—	—
1995-03-30	-93	C363	1.5A	—	—	—	—	—	—	—	—	—	—	—	—	1418	< 6.6	—	—
1995-04-16	-76	C418	6C	—	—	—	—	—	—	—	—	—	—	2768	< 1.1	1418	< 1.2	—	—
1995-05-27	-35	C204a	1.5B	—	—	—	—	—	—	8640	< 0.3	4800	< 0.2	—	—	—	—	—	—
1995-05-27	-35	C204a	1.5B	—	—	—	—	—	—	8640	< 0.3	4800	< 0.5	—	—	—	—	—	—
1995-06-07	-24	C204a	750C	—	—	—	—	—	—	8640	< 0.8	4800	< 0.3	—	—	—	—	—	—
1995-06-07	-24	C204a	750C	—	—	—	—	—	—	8640	< 0.3	4800	< 0.2	—	—	—	—	—	—
1995-07-27	26	C204c	6C	—	—	—	—	—	—	—	—	—	—	2368	< 1.3	1376	< 3.4	—	—
1995-08-03	33	C363	375	—	—	—	—	—	—	—	—	—	—	—	—	1418	< 16.7	—	—
1996-02-06	220	CT09	750B	—	—	—	—	—	—	—	—	—	—	—	—	1664	< 1.5	—	—
1996-08-01 (1)	397	C466	6C	—	—	—	—	—	—	8640	0.5 ± 0.0	4800	< 1.0	—	—	—	—	—	—
1996-12-05 (2)	523	C505	365	—	—	—	—	—	—	—	—	—	—	2368	< 0.4	1384	< 0.7	—	—
1996-12-15 (2)	533	C586	6D	—	—	—	—	—	—	8512	1.9 ± 0.1	4928	1.8 ± 0.1	—	—	—	—	—	—
1996-12-15 (2)	533	C586	6D	—	—	—	—	—	—	8512	2.3 ± 0.1	4928	1.8 ± 0.1	—	—	—	—	—	—
1997-06-17	717	V100C	6A	—	—	—	—	—	—	8425	15.4 ± 0.3	—	—	—	—	—	—	—	—
1997-06-17	717	V100C	6A	—	—	—	—	—	—	8425	13.7 ± 0.3	—	—	—	—	—	—	—	—
1997-12-05 (3)	888	V099	6C	—	—	—	—	—	—	—	—	—	—	2268	27.2 ± 2.1	—	—	—	—
1997-12-05 (3)	888	V099	6C	—	—	—	—	—	—	—	—	—	—	2268	21.9 ± 1.1	—	—	—	—
1997-12-31 (3)	914	C694	6C	—	—	—	—	—	—	6024	134.0 ± 13.1	4800	129.0 ± 8.6	—	—	—	—	—	—
1999-06-19 (4)	1449	C788	375	—	—	—	—	—	—	—	—	—	—	—	—	1418	85.2 ± 2.1	—	—
1999-06-19 (4)	1449	C788	375	—	—	—	—	—	—	—	—	—	—	—	—	1384	78.9 ± 1.5	—	—
2000-06-19 (4)	1815	V137	6B	—	—	—	—	22215	68.9 ± 8.5	—	—	—	—	—	—	—	—	—	—
2000-06-19 (4)	1815	V137	6B	—	—	—	—	22203	72.4 ± 9.1	—	—	—	—	—	—	—	—	—	—
2000-06-19 (4)	1815	V137	6B	—	—	—	—	22190	76.4 ± 10.0	—	—	—	—	—	—	—	—	—	—
2002-07-18	2574	V137	1.5G	—	—	—	—	22224	69.5 ± 8.8	—	—	—	—	—	—	—	—	—	—
2002-07-18	2574	V137	1.5G	—	—	—	—	22216	70.8 ± 5.6	—	—	—	—	—	—	—	—	—	—
2002-07-18	2574	V137	1.5G	—	—	—	—	22201	61.8 ± 8.7	—	—	—	—	—	—	—	—	—	—
2002-07-18	2574	V137	1.5G	—	—	—	—	22187	71.9 ± 8.6	—	—	—	—	—	—	—	—	—	—
2002-07-18	2574	V137	1.5G	—	—	—	—	22172	62.7 ± 8.2	—	—	—	—	—	—	—	—	—	—
2003-09-07 (5)	2990	C1224	EW367	—	—	—	—	23659	72.0 ± 7.4	—	—	—	—	—	—	—	—	—	—
2003-11-03 (5)	3047	C1049	H214	—	—	—	—	19008	77.1 ± 7.8	—	—	—	—	—	—	—	—	—	—
2003-11-03 (5)	3047	C1049	H214	—	—	—	—	16960	86.2 ± 9.4	—	—	—	—	—	—	—	—	—	—
2003-11-04 (5)	3048	C1049	1.5D	—	—	—	—	22796	72.5 ± 7.1	—	—	—	—	—	—	—	—	—	—
2003-11-04 (5)	3048	C1049	1.5D	—	—	—	—	21056	69.2 ± 7.4	—	—	—	—	—	—	—	—	—	—
2003-11-08 (5)	3052	C1049	1.5D	—	—	—	—	—	—	8256	163.0 ± 7.3	5056	236.0 ± 4.5	—	—	—	—	—	—
2004-04-02 (6)	3198	C1424	6A	—	—	—	—	—	—	8640	162.0 ± 1.3	4800	240.0 ± 1.1	2368	364.0 ± 2.7	1384	481.0 ± 7.5	—	—
2004-05-20 (6)	3246	CX065	1.5B	—	—	—	—	22087	66.1 ± 9.2	—	—	—	—	—	—	—	—	—	—
2004-06-13 (6)	3270	V176	750D	—	—	—	—	22209	56.8 ± 10.3	—	—	—	—	—	—	—	—	—	—
2004-06-13 (6)	3270	V176	750D	—	—	—	—	22195	59.3 ± 11.7	—	—	—	—	—	—	—	—	—	—
2004-08-01 (6)	3319	V176B	H168	—	—	—	—	22209	65.7 ± 8.8	—	—	—	—	—	—	—	—	—	—
2004-08-01 (6)	3319	V176B	H168	—	—	—	—	22195	65.6 ± 8.1	—	—	—	—	—	—	—	—	—	—
2005-03-14 (7)	3544	C1368	H214	—	—	—	—	22193	66.7 ± 7.8	—	—	—	—	—	—	—	—	—	—
2005-04-20 (7)	3581	C1368	750A	—	—	—	—	22194	85.6 ± 20.1	—	—	—	—	—	—	—	—	—	—
2005-05-25 (7)	3616	C1321	Hybrid	88632	23.9 ± 6.0	—	—	—	—	—	—	—	—	—	—	—	—	—	—
2005-10-27 (7)	3771	C1049	H168	—	—	—	—	18752	70.8 ± 9.2	—	—	—	—	—	—	—	—	—	—
2005-10-27 (7)	3771	C1049	H168	—	—	—	—	21056	58.4 ± 10.8	—	—	—	—	—	—	—	—	—	—
2005-11-13 (7)	3788	C1049	1.5C	—	—	—	—	—	—	8640	161.0 ± 2.2	4800	246.0 ± 1.7	—	—	—	—	—	—
2006-04-29 (8)	3955	C1049	H214	—	—	—	—	18752	76.4 ± 7.3	—	—	—	—	—	—	—	—	—	—
2006-04-29 (8)	3955	C1049	H214	—	—	—	—	21056	69.2 ± 7.3	—	—	—	—	—	—	—	—	—	—
2006-06-08 (8)	3995	CX114	1.5D	—	—	—	—	22193	70.8 ± 9.0	—	—	—	—	—	—	—	—	—	—
2006-06-08 (8)	3995	CX114	1.5D	—	—	—	—	20160	75.7 ± 7.6	—	—	—	—	—	—	—	—	—	—
2006-06-21 (8)	4008	C1049	1.5D	—	—	—	—	—	—	8640	161.0 ± 7.1	4800	239.0 ± 6.0	—	—	—	—	—	—

A stellar autopsy of the radio-bright SN 1996cr

Table 1 (cont'd)

Obs. Date	Days from explosion	Obs. ID	Array	W-Band		K _a -Band		K-Band		X-Band		C-Band		S-Band		L-Band		U-Band	
(1)	(2)	(3)	(4)	ν	S_ν	ν	S_ν	ν	S_ν	ν	S_ν	ν	S_ν	ν	S_ν	ν	S_ν	(19)	(20)
2006-09-14 ⁽⁸⁾	4093	C1341	H75	—	—	—	—	—	—	—	—	—	—	—	—	1384	479.0 ± 2.5	—	<i>C. Meunier et al.</i>
2006-09-14 ⁽⁸⁾	4093	C1341	H75	—	—	—	—	—	—	—	—	—	—	—	—	1418	505.0 ± 3.2	—	
2007-06-24	4376	VX013A	EW352	—	—	—	—	22316	69.4 ± 7.7	—	—	—	—	—	—	—	—	—	
2007-06-24	4376	VX013A	EW352	—	—	—	—	22348	66.8 ± 9.0	—	—	—	—	—	—	—	—	—	
2008-04-21 ⁽⁹⁾	4678	C1803	6A	—	—	—	—	—	—	8640	144.0 ± 4.0	4800	210.0 ± 4.0	2368	311.0 ± 11.0	1384	423.0 ± 27.3	—	
2008-08-16 ⁽⁹⁾	4795	C1750	6B	—	—	—	—	22192	63.0 ± 9.0	—	—	—	—	—	—	—	—	—	
2008-10-02 ⁽¹⁰⁾	4842	C184	H168	—	—	34496	40.3 ± 6.0	—	—	—	—	—	—	—	—	—	—	—	
2008-10-12 ⁽¹⁰⁾	4852	C184	6A	—	—	—	—	—	—	8640	128.0 ± 20.0	4786	197.0 ± 20.1	—	—	—	—	—	
2008-10-12 ⁽¹⁰⁾	4852	C184	6A	—	—	—	—	—	—	—	—	—	—	2496	293.0 ± 39.8	1376	405.0 ± 71.0	—	
2008-12-22 ⁽¹¹⁾	4923	C184	6C	—	—	—	—	—	—	8640	131.0 ± 21.0	4786	196.0 ± 19.0	2496	273.0 ± 23.0	1376	421.0 ± 65.0	—	
2009-01-25 ⁽¹²⁾	4957	-	MOST	—	—	—	—	—	—	—	—	—	—	—	—	—	—	843	
2009-01-28 ⁽¹²⁾	4960	C184	1.5C	—	—	—	—	—	—	8640	134.0 ± 10.3	4786	194.0 ± 13.0	2496	296.0 ± 32.0	1376	438.0 ± 60.0	520.0 ± 30.0	
2009-04-13 ⁽¹³⁾	5035	CX172	H168	—	—	—	—	—	—	8800	126.0 ± 9.1	5500	186.0 ± 8.9	—	—	—	—	—	
2010-01-16 ⁽¹⁴⁾	5313	C1726	6A	—	—	—	—	—	—	9000	116.0 ± 10.7	5500	156.0 ± 9.9	—	—	—	—	—	
2010-05-05 ⁽¹⁴⁾	5422	V253	H214	—	—	—	—	22000	48.0 ± 5.3	—	—	—	—	—	—	—	—	—	
2010-05-07 ⁽¹⁴⁾	5424	V253	H214	—	—	—	—	—	—	8425	106.0 ± 28.1	—	—	—	—	—	—	—	
2011-05-09	5791	C2479	1.5B	—	—	—	—	—	—	—	—	—	—	2100	244.0 ± 8.5	1418	330.0 ± 40.1	—	
2011-05-09	5791	C2479	1.5B	—	—	—	—	—	—	—	—	—	—	2100	251.0 ± 6.3	1613	310.0 ± 29.9	—	

Note. — *Column 1:* Starting date of observation. Numbers in parenthesis indicate epochs whose data were combined, as described in Sec. 3.2. *Column 2:* Days from explosion date. *Column 3:* Observing program ID. *Column 4:* Array configuration. *Columns 5, 7, 9, 11, 13, 15, 17, and 19:* Mean frequency of observed band in units of MHz. *Columns 6, 8, 10, 12, 14, 16, 18, and 20:* Integrated flux densities, as determined from IMFIT, or 3σ upper limits, as determined from IMSTAT, in units of mJy. Uncertainties include both statistical and systematic error terms. The systematic error is estimated from the ratio of the measured calibrator fluxes over its estimated historical value based on monitored light curves (typical variance was 5–20%).

G. Meunier et al.

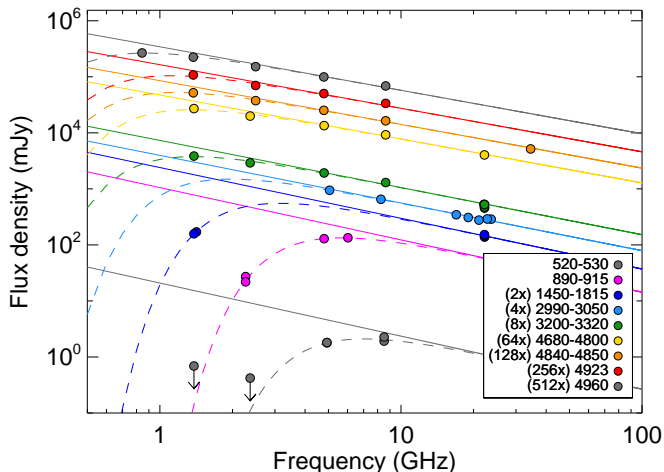


Figure 3. Radio spectra of SN 1996cr for selected epochs indicated in the legend as days after explosion. Flux densities (filled circles) are shown with 1σ error bars (which are smaller than symbols in some cases) or 3σ upper limits (downward arrows). The intrinsic and absorbed spectra are represented by solid and dashed lines respectively, with the latest spectra at the top. For clarity, fluxes are plotted with the multiplicative factors in parenthesis. Early-time spectra show high absorption, mostly affecting the lower frequencies as expected from FFA. The effect of adopting a varying spectral index (see §3.2 and Fig. 4) can be seen in the intrinsic models plotted at each epoch.

3.2 Empirical Radio Properties

A key constraint on the nature of the radio emission is its spectral index. Measuring this for SN 1996cr, however, is non-trivial, since this object was largely observed via serendipitous observations with sparse frequency coverage, while additionally the data during the first 1000 days appear to be heavily absorbed (Fig. 3). In order to deal with the lack of multifrequency observations at each epoch, the available data were grouped together in periods of up to six months where possible, during which the spectral index is assumed to remain constant to within our measurement errors.

A constant spectral index is generally assumed for radio SNe, but the data for SN 1996cr allow us to confront this assumption directly. We note that the late-time data for SN 1996cr, between days ~ 2800 – 5000 , exhibit minimal absorption, and thus provide relatively strong constraints on the intrinsic spectral index. For epochs with wide frequency coverage, an FFA optical depth and spectral index were computed using the Levenberg-Marquart least-squares method. Limits on the optical depth for epochs with poor low-frequency coverage were set equal to the value from the last well-fit spectrum. These limits are of minimal consequence, as the free-fit spectral indices in epochs where such optical depth limits exist only show marginal variations to changes in the limiting optical depth values. The constraints on the optical depths and the values of the spectral indices are listed in Table 2.

As seen in Fig. 4, well constrained values of the intrinsic spectral index between days ~ 3000 – 5000 appear to shift to flatter values at later times, and a weighted linear regression fit (OLS $Y|X$; Isobe et al. 1990) to the values of the spectral

index shows evidence for mild spectral flattening (nominally $\sim 10\sigma$ confidence), which we assume to be the intrinsic variation of the spectral index. A constant alpha model, however, cannot be ruled out using χ^2 or likelihood ratio statistics (only $\sim 1.5\sigma$ confidence), leaving doubts about the veracity of the trend. Extrapolation of this trend back to days ~ 520 , ~ 900 and ~ 1600 – 1900 is consistent with the data, although these values are not well constrained due to stronger degeneracies between their spectral indices and absorption.

We characterise the evolution of the intrinsic spectral index of SN 1996cr in a manner similar to that used for SN 1987A in Zanardo et al. (2010). The intrinsic spectral index is given by $\alpha(t) = \alpha_0 + \beta_0 \times (t - t_0)/\Delta$, where t is given in days, $t_0 = 3000$ d, $\Delta = 365.25$ d, $\alpha_0 = 0.852 \pm 0.002$, and $\beta_0 = -0.014 \pm 0.001$. Errors on regression parameters were assessed through jackknife resampling. We extrapolate this regression back to day 400 (see Fig. 4) and rely on the fixed values of the spectral index from the above fit to reassess values of the optical depth that will be used in the subsequent analysis. The specific (fixed) values of the spectral index and the refitted values of the optical depth are also listed in Table 2.

The mild evolution of the spectral index of SN 1996cr is similar to that of the highly monitored SN 1987A (Zanardo et al. 2010). Fig. 4 also shows the spectral index variation for SN 1993J; we note that Weiler et al. (2007) assumed a constant spectral index for this SN, but its spectral index clearly appears to vary based on fig. 4 of Weiler et al. (2007), fig. 7 of Chandra et al. (2004), and fig. 8 of Martí-Vidal et al. (2011). From the data in the ~ 80 – 3000 d period from Weiler et al. (2007), a constant spectral model is rejected at a 100% confidence level. We characterise a varying spectral model for SN 1993J as $\alpha = 0.865 \pm 0.003$ at day 800, and a decay rate of $\Delta\alpha = -0.036 \pm 0.001 \text{ yr}^{-1}$.

It is intriguing that the spectral indices of arguably the three best-studied radio SNe all show evidence for spectral flattening with time. This variation runs counter to some theoretical predictions (e.g., Ellison et al. 2004; Berezhko & Ksenofontov 2006; Tatischeff 2009) and clearly warrants further investigation. It is still unclear whether this spectral flattening is a ubiquitous property of young RSNe. For instance, SN 1979C also has a considerable amount of radio data available and appears to remain constant since day 2000 (see fig. 3 of Montes et al. 2000), although difficulties associated with disentangling spectral and CSM variations and the large scatter in measured spectral indices could easily mask subtle spectral changes such as those observed in Fig. 4. SN 1986J, on the other hand, shows strong, complex spectral variations with time. VLBI observations suggest that these variations appear to stem from the flat spectrum of the remnant core brightening as the steep spectrum of the shell fades (Bietenholz et al. 2010). Thus neither SN 1979C nor SN 1986J provide ‘clean’ examples. Other RSNe, such as SN 1980K and SN 1994I show hints of spectral variations, while SN 1978K, SN 1995N and SN 2001ig remain thoroughly ambiguous (Montes et al. 1998; Weiler et al. 2011; Smith et al. 2007; Chandra et al. 2009; Ryder et al. 2004); unfortunately, all are relatively weak radio sources and hence too poorly constrained to provide compelling examples either for or against spectral flattening. Clearly interpreting mild evolutionary trends (e.g., SN 1993J) should be done with caution, given the obvious

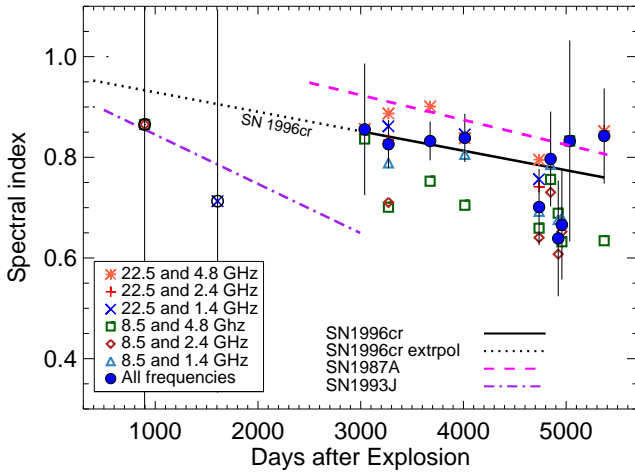


Figure 4. Points show the intrinsic spectral indices and 1σ errors derived from linear regression fits to the SN 1996cr spectra shown in Fig. 3. Also shown are all available two-frequency spectral indices for a given epoch (errors are not shown for plot clarity, but can be assessed using Table 1). A linear regression fit to the well constrained spectral indices from days 3000–5000 versus time suggests that the spectral slope may be flattening, similar to the spectral index variations seen in both SN 1987A and SN 1993J (see text for details), although the result is not yet robust. Early best-fitting spectral indices for SN 1996cr are not included in this parametrisation, but are consistent with our extrapolation of the best-fitting time evolution to within their large errors.

degeneracies between parameters responsible for the synchrotron spectrum in SNe. Past and future LBA imaging can marginally resolve SN 1996cr and could highlight any strong spectral variations in this source (Bartel et al., in preparation).

The brightness temperature of SN 1996cr, which is calculated from the simulated shock expansion and the FFA-corrected data, does not exceed the value of $\approx 2\text{--}4 \times 10^{11}$ K (there is a very weak frequency dependence) which typically leads to SSA (Readhead 1994). However, this limit may be reached for hypothetical low frequency data points around day 800, which suggests a possible combination of FFA and SSA at early times, although this is not well constrained with our limited data. We model this in more detail in the next section.

3.3 Hydrodynamical Simulation

We based our work on the 1-dimensional hydrodynamical simulations by Dwarkadas et al. (2010) which provides the hydrodynamic and kinetic information of the ejecta-CSM interaction. Without detailed calculations and an examination of the microscopic physics, which is beyond the scope of this paper, it is impossible to calculate the behaviour of the magnetic field and the acceleration of particles to relativistic energies that dictate the strength of the synchrotron emission. One must therefore appeal to simpler scaling relations to infer the behaviour of these quantities in terms of others that are well understood. Chevalier (1996) has outlined several possibilities for how the synchrotron luminosity pa-

rameters might scale, although many other variations may exist. The radiating electron energy density ($\propto K$) and the magnetic energy density ($\propto B^2$) may scale with the thermal energy density ($\propto P$), since these are thought to be built up by high-pressure turbulent motions in the shock, or may also scale with the thermal particle density if a constant fraction of the thermal particle density is injected in the acceleration process. Another possibility is that the magnetic energy density may decrease as the surface area ($B^2 \propto r^{-2}$), as the magnetic field is carried out from the surface of the progenitor via the wind. These simple physical scalings, however, may not provide a complete picture of the likely complex physics involved, as evidenced by the spectral index flattening and the decoupling of the X-ray and radio light curves in SN 1987A, for instance. Although there is a physical basis for the possible energy density scalings, the only SN in which such scaling relations have been successfully constrained (albeit somewhat controversially) is SN 1993J (e.g., Fransson & Björnsson 1998; see also Mioduszewski et al. 2001 for alternative viewpoint), where the magnetic energy density was derived independently from SSA through very early monitoring, and radius constraints were provided by VLBI data (e.g., Marcaide et al. 1997; Bartel et al. 2000), thus removing several of the degeneracies that force the need for the scaling relations in the first place. We discuss the results of applying a few particular scaling models in Sec. 4.2.

As mentioned in the previous section, SSA should play a role in the spectral appearance of SN 1996cr at very early times. To incorporate SSA into our radio models in a self-consistent way, we first determined the unabsorbed brightness temperature for each frequency of our radio model vs. time, assuming a spherical shell morphology that evolves with the shock radius. We then applied SSA to the full radio model assuming $\tau_{\text{SSA}} \sim 1$ at the critical frequency where the brightness temperature surpassed $\approx 3 \times 10^{11}$ K (Readhead 1994). Therefore, the radio model is absorbed by this model-dependent SSA, in addition to FFA whose constraints on τ_{FF} are presented in Table 2.

4 RESULTS

We initially characterise the ionised region surrounding SN 1996cr and compare the radio constraints on the CSM free electron density to the expectations from hydrodynamic simulation. The simulated radio light curves are then presented for a few basic scaling models, and are evaluated by comparing their individual features to those of the observed light curves. These results set the scope for further research on this object.

4.1 Empirical Constraints on the CSM

The constraints on the FFA optical depth allow for the study of the CSM ionisation by providing limits on the density of free electrons. This in turn can be used as a relatively direct cross-check on the simulation density distribution, since the free electron density provides a strong lower limit on the total mass in the CSM assuming full ionisation. For simplicity, we considered a CSM composition of H only, and adopted a scaling factor of 20 (based on the X-ray derived abundances

Table 2. Selected epochs with corresponding free-fit optical depth and spectral index, final optical depth, and fixed spectral index.

Days since explosion	τ_0 ($\text{K}^{-1.35} \text{ pc cm}^{-6}$) (free-fit)	Spectral Index (free-fit)	τ_0 ($\text{K}^{-1.35} \text{ pc cm}^{-6}$) (refitted)	Spectral Index (fixed)
397	30.00 †	1.00 †	30.00 †	0.95
530*	28.16 ± 2.56	1.00 †	27.07 ± 2.54	0.95
897*	16.67 ± 4.97	0.87 ± 0.86	17.05 ± 0.51	0.93
1607*	3.75 ± 2.11	0.71 ± 0.38	4.82 ± 0.16	0.91
3039*	1.87 ± 5.20	0.86 ± 0.13	1.66 ± 1.60	0.85
3270*	0.72 ± 0.23	0.83 ± 0.05	0.78 ± 0.13	0.84
3676	0.70 †	0.83 ± 0.04	0.70 †	0.83
4013	0.73 ± 0.18	0.84 ± 0.05	0.64 ± 0.06	0.81
4737*	0.39 ± 0.34	0.70 ± 0.08	0.70 ± 0.19	0.79
4849*	0.58 ± 0.58	0.80 ± 0.09	0.51 ± 0.40	0.78
4923*	0.15 †	0.64 ± 0.12	0.46 ± 0.41	0.78
4959*	0.13 ± 0.15	0.67 ± 0.11	0.27 ± 0.06	0.78
5035	0.10 †	0.83 ± 0.20	0.10 †	0.77
5370	0.10 †	0.84 ± 0.09	0.10 †	0.76

Note. — Only epochs marked with an asterisk are used in the subsequent analysis, as they provide the most reliable constraints on the refitted optical depth. Values marked with † denote instances where the parameter pegged at the reasonable imposed upper or lower limits that we set in the fitting routine; the corresponding parameter (τ_0 or spectral index α) was therefore evaluated at this fixed value and its errors should be regarded with caution.

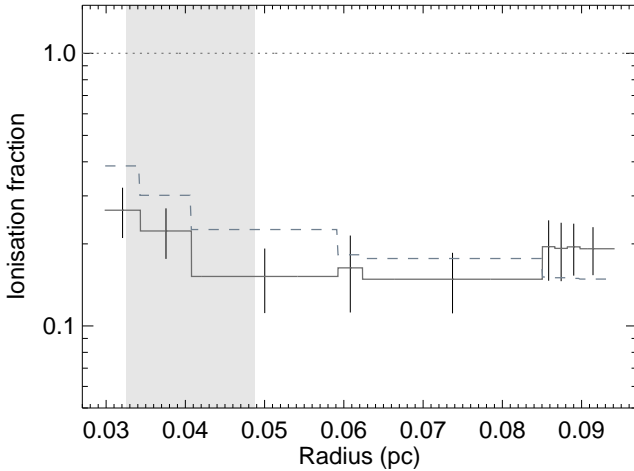


Figure 5. The CSM ionisation fraction and 1σ error computed from constraints on the FFA optical depth (solid line), and the theoretical ionisation fraction for comparison (dashed line), for a CSM temperature of 10^4 K. The presumed location of the dense shell is denoted by the gray-shaded region.

and resulting mean molecular weight of the CSM) to scale our results to the CSM composition of H, He and metals presented for SN 1996cr in Dwarkadas et al. (2010).

Each observation epoch has an approximately corresponding time step in the simulation, and a shock radius is assigned to it based on the position of the forward shock at that time. The free electron density in front of the shock can be determined from the difference in the values of the optical depth between two radio epochs (Eq. 2). This requires setting a value N_e for the outermost shock radius

(latest radio epoch) from which to iterate back through the CSM to the innermost shock radius (earliest radio epoch), which we assumed to be $N_e = 10^4 \text{ cm}^{-3}$, corresponding to an average value found in HII regions. We adopt this value since SN 1996cr appears to reside at the centre of a diffuse H α clump 5–10 pc in diameter (cf. figs. 3 and 5 of Bauer et al. 2008), which is presumably a large extended HII region ionised by several massive stars. For simplicity, we assumed that the CSM has a uniform temperature, and investigated a range of initial CSM temperatures between $T = 10^4$ – 10^6 K, since these were not directly constrained by the hydrodynamical simulation. This range should be appropriate for a wide range of RSG wind densities (e.g., Fransson & Björnsson 1998 and references therein). Such temperature variations will lead to proportionally higher ionisation fractions, although the radial form appears to remain relatively steady. The shock radii and constraints on N_e are listed in Table 3 for $T = 10^4$ K. The number densities of total electrons that are available to be ionised are obtained from the simulation over the same CSM regions delimited by the radio epochs. Finally, the CSM ionisation fraction is calculated directly from the free and total electron densities, and is shown in Fig. 5.

The radio-constrained free electron densities appear fully in line with (i.e., lower than) the total electron densities from the hydrodynamical simulation for temperatures lower than 10^5 K. Overall, the CSM ionisation fraction decreases slightly with radius; this is fully consistent with our expectations, based on recombination after a strong flash ionisation from the SN outburst ionising our adopted CSM density distribution. We are relatively confident in our adopted value of N_e for the latest radio epoch, as all values lower than $5 \times 10^4 \text{ cm}^{-3}$ appear stable, yielding ionisation fractions that are consistent with the simulation, while values over

Table 3. Selected epochs with corresponding shock radii and constraints on N_e , determined from the hydrodynamic simulation and constraints on the FFA optical depth.

Days since explosion	Radius (10^{17} cm)	N_e (10^4 cm $^{-3}$)
530	0.918	(2.59 ± 0.16)
897	1.058	(2.14 ± 0.14)
1607	1.256	(1.32 ± 0.23)
3039	1.825	(1.06 ± 0.26)
3270	1.921	(0.94 ± 0.14)
4737	2.620	(1.05 ± 0.16)
4849	2.667	(1.03 ± 0.14)
4923	2.717	(1.03 ± 0.08)
4959	2.766	1.00

this tend to drive the ionisation in all shells to significantly higher ionisation fractions.

As an additional check, we obtain the CSM neutral fraction directly from the ionised fraction, and use it to calculate the neutral hydrogen column, which we then compare to the one obtained from spectral fits to the X-ray data. Between 1999 June (~ 1450 d) and 2009 January (~ 5000 d), the CSM neutral fraction implies a neutral hydrogen column density of $N_H = (9.3 \pm 2.2) \times 10^{20}$ amu cm $^{-2}$, which is roughly consistent with a physical measurement of $N_H = 1.8 \times 10^{21}$ amu cm $^{-2}$ presented in Dwarkadas et al. (2010), based on differential spectral fits to the 2000 and 2009 HETG data. Although there may be a slight difference in the regions being considered for both these column densities, it is perhaps more likely that these values differ as a result of the latter being constrained by model fits to the X-ray spectrum, which can be easily affected by low-energy spectral lines.

We can also crudely estimate the evolution of the CSM ionisation following shock breakout on theoretical grounds to obtain an interesting consistency check with the hydrodynamic simulation. A SN explosion with an average output energy of $\sim 10^{51}$ erg will radiate $(0.5\text{--}2.3) \times 10^{57}$ ionising photons during the first 1.5 days (Ensmann & Burrows 1992), which at the higher end is sufficient to ionise up to $\sim 2M_\odot$ of material (Lundqvist & Fransson 1996), assuming the CSM is pure H. The CSM mass in the hydrodynamic simulation is about $2.1M_\odot$, and thus could possibly be almost completely ionised by the shock breakout. We therefore assume that the entire model CSM is initially ionised, which provides an upper bound on the true ionisation of the CSM; the true CSM is likely to be less ionised if it is not distributed in a spherically symmetric manner, has a mass significantly higher than $2M_\odot$, or the explosion energy is lower. We model the recombination using the initial CSM density distribution from the hydrodynamical simulation (for which we assume a CSM composition of pure H, and scale to a composition of H, He and metals with our assumed scaling factor) and the HII recombination rates given in Seager et al. (2000, i.e., $\alpha_B = 2.6 \times 10^{-13}$ cm 3 s $^{-1}$ for our assumed CSM temperature). As two examples, we note that the CSM densities of free electrons at 0.04 pc (within the shell) and 0.12 pc (within the assumed RSG wind) are 1.5×10^6 and 6×10^4 cm $^{-3}$, and will completely recombine in 0.08 and 2.1 yrs, respectively.

The X-ray radiation from the SN shock provides an ongoing source of energy for reionisation of recently recombined material. To model the amount of ionising photons that the shock injects into the CSM as a function of time, we assume that the ionising photon rate scales linearly with the X-ray light curve. Using the same absorbed non-equilibrium ionisation model adopted in Dwarkadas et al. (2010), we normalised the photon rate to 2.7×10^{48} photons s $^{-1}$ on day ~ 1670 to match the absorbed photon rate from the 2001 August XMM spectrum. Our simulation shows that as the shock moves through the CSM, it largely reionises the immediate region around it (i.e., the bin it is in), but nothing more. Thus, the vast majority of the line-of-sight ionisation we observe comes from the initial shock-breakout ionisation. The resulting CSM ionisation fraction is shown for comparison in Fig. 5. From this model, the theoretical neutral column density in the 1450–5000 d period is $N_H = (9.4 \pm 1.9) \times 10^{20}$ amu cm $^{-2}$, in accord with the value from the HETG 2000–2009 data.

4.2 Simulation of the Radio Light Curve

As a test of our methods, we initially computed radio light curves for a hydrodynamic simulation of a self-similar shock expansion to demonstrate that we could correctly reproduce the decline rates of the synchrotron luminosity presented in Chevalier (1996) for the different models therein. We then applied this code to the more complex simulation of Dwarkadas et al. (2010), scaling the simulated light curves to the radio data.

For SN 1996cr there are three conditions that the observations require if the model is to successfully simulate the light curve. (1) Low emission while the ejecta is moving within the sparse cavity, since we have upper limits for this from both X-rays and radio. (2) A sharp increase in flux from ~ 700 to ~ 1000 d, as the SN ejecta initially impacts and interacts with the dense shell. The fluxes in the 4.8 and 8.5 GHz bands rise together, which indicates that the rise is intrinsic rather than the result of diminishing absorption, since FFA (or SSA for that matter) will affect the bands differently. (3) A flattening of the light curve between days ~ 1000 and ~ 4000 , with the beginning of a decrease/turnover at very late times.

Fig. 6 shows the simulated radio light curves for two different models. The standard model in Chevalier (1996), relating K and B^2 to the thermal energy density, proved inadequate in our simulations. It provides a fair match to the luminosity rise around day 700, but the subsequent peak in luminosity decreases too quickly as the forward shock leaves the shell. The second model, which relates K to the thermal particle density and B^2 to the surface area, does a better job at fitting the late-time data, but fails however to fit the data from the rise, since the simulated flux around day 900 is almost one order of magnitude lower than the observations. In our model we have assumed that the radio emission is generated from both the forward and reverse shocks, as the forward shock-only light curve resulted in poor fits to the data (i.e., lack of plateau region followed by a sharp falloff).

More complex scalings may allow us to potentially fit the entire radio light curve, but remain ad hoc due to our currently poor understanding of the detailed microphysics that ultimately drives the large-scale radio emission. This

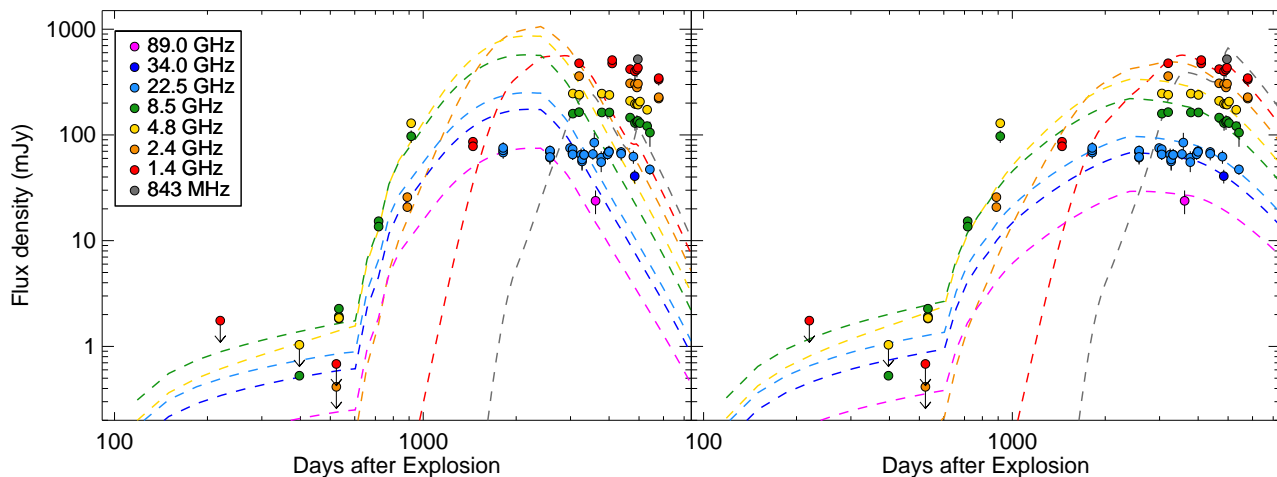


Figure 6. Simulated light curves (lines) and observed radio flux densities (circles) for SN 1996cr. Left: The ‘standard’ model scales K and B^2 as the thermal energy density (erg cm^{-3}). We fixed the constants of proportionality for the K and B^2 scalings at a radius of 10^{16} cm to be $\approx 3.4 \times 10^{-5}$ and ≈ 1.3 respectively, so as to best fit the data. This model provides an intrinsic flux rise at ~ 700 d but fails to match the late-time plateau region. Right: K scales as the thermal particle density (cm^{-3}) and B^2 scales as the surface area (cm^{-2}). The constants of proportionality for K and B^2 at a radius of 10^{16} cm are fixed to $\approx 4.2 \times 10^{17}$ and $\sim 10^{26}$ respectively. Although the simulated light curve provide a better match to the late-time data, the flux at day ~ 900 is nearly an order of magnitude lower than observations.

obviously makes it difficult to assess whether the deviations between radio data and models stem from our simplistic approach, which assumes that the emission at all times and all locations arises from both shocks, or alternatively, may still be limited by the hydrodynamic simulation. While the simulation has some difficulty reproducing a similar feature in the X-ray light curve (Dwarkadas et al. 2010), it is able to reproduce the X-ray spectra and light curves, which are more directly and fundamentally tied to physical parameters (e.g., density, emissivity, and ionisation equilibrium), and even allow to separate X-ray emission from the forward shock, which dominates during the first seven years, and reverse shock, which dominates thereafter. Our radio calculations, on the other hand, do not allow this level of accuracy or differentiation.

5 DISCUSSION & CONCLUSIONS

We have presented an up-to-date sequence of radio light curves of SN 1996cr. Using an analytic model that describes the radio emission from SNe, combined with a hydrodynamic simulation of the synchrotron-emitting regions, we simulated the observed radio light curves of SN 1996cr to further constrain the density of the CSM, particularly in the sparse region interior to the shell, for which there are no firm X-ray constraints implemented in the hydrodynamic simulation.

To this end, we explored some basic scalings that relate the hydrodynamics of the shock to the magnetic field and the radiating electron distribution that are required for synchrotron emission. For all of the models studied, we found that the behaviour in certain periods of our simulated radio light curves matched the functional form of our observations relatively well, but invariably failed to match the most tightly constraining temporal features, typically

the rise around ~ 700 d and/or the plateau region between ~ 2000 – 5000 d.

The simulation shown on the right panel in Fig. 6 (with $K \propto$ thermal particle density and $B^2 \propto$ surface area) matches the radio light curves reasonably well from a radius of ≈ 0.04 pc outwards. The different scalings that we studied have their share of assumptions and potential failings. However, the mismatch interior to ≈ 0.04 pc coincides with the lack of strong constraints on the simulation parameters from the X-ray light curve at similar radii, which may mean that the inner region of the dense shell is not being adequately modelled. To improve the early discrepancies, we need to understand how the magnetic field and accelerated particle distribution actually scale as the SNe shock collides with a dense CSM shell, and/or have the simulation potentially consider (1) a more concentrated shell mass along the inner edge, (2) clumpy structure that could provide modifications to both the ionisation and radio flux, (3) asymmetric mass distribution to spread out/flatten the peak, or (4) modification to the SN parameters (e.g., ejecta density slope, the ejecta mass and explosion energy). Changes to the simulations, however, cannot be too large, since the non-equilibrium ionisation model spectra already match the HETG X-ray spectra well over several epochs.

Geometrical considerations, such as possible asymmetries in the wind, in the SN explosion or in the dense shell, were not included in our calculations. Dewey et al. (2011) recently showed that SN 1996cr might in fact not be spherically symmetric. Nevertheless, our assumption that a 1D hydrodynamic simulation is appropriate to simulate the radio light curve is at least justified by the fact that it also reproduces the broad features of the observed X-ray light curve (Dwarkadas et al. 2010).

Of course, the X-ray emission is thermal, while the radio emission is non-thermal synchrotron. These are very different mechanisms, arising from potentially distinct regions

and scaling with different physical parameters; the microphysics and mechanics of which are poorly understood or constrained in the radio. Thus we should not be surprised to see a decoupling of the simulated X-ray and radio light curves. Clearly, the physics that generates the X-ray emission is much simpler than that of the radio, as it relates only to the density, emissivity, and ionisation (in)equilibrium of the emitting material. This close link between the hydrodynamical parameters of the shock and a correct simulation of the observed X-ray light curve lends more support to the hydrodynamic simulation as accurately descriptive of the dynamics of the shock. We attempted to simulate the radio light curve using simple assumptions for the magnetic field and the electron distribution, which do not appear to be appropriate for complex objects such as SN 1996cr. The use of simple scaling relations, combined with hydrodynamic simulations, also failed to adequately reproduce the sharp rise and subsequent linear increase of radio emission in SN 1987A (Dwarkadas 2007b,c). These are precautions to be considered when trying to constrain the circumstellar density of these objects using simple radio models, because even if an X-ray-based density model is available, it may not be able to accurately model the radio light curve while avoiding the degeneracies that arise in trying to determine viable density scalings.

SN 1996cr remains quite bright at nearly all wavelengths, and future radio and X-ray monitoring will be able to constrain the apparent decline, which should place stronger constraints on the outer wind and CSM density distribution. Future monitoring with the LBA and ALMA will be able to resolve the radio morphology of SN 1996cr in greater detail to constrain its spatial expansion (i.e., current velocity) and emission regions.

ACKNOWLEDGMENTS

CM and FEB would like to thank Andrés Jordán for suggestions. Special thanks to Juergen Ott for providing the 89 GHz reduced data and Shari Breen for early access to her data. We acknowledge support from CONICYT-Chile under grants FONDECYT 1101024 (CM, FEB), alma-conicyt 31100004 (FEB), and fondap-cata 15010003 (FEB), Basal-CATA grant PFB-06/2007 (FEB), the Iniciativa Científica Milenio through the Millennium Center for Supernova Science grant P10-064-F with input from "Fondo de Innovación para la Competitividad, del Ministerio de Economía, Fomento y Turismo de Chile" (FEB), and Chandra X-ray Center grants SAO GO9-0086, GO0-11095, and GO1-12095B (FEB, VVD).

FEB thanks the ATNF Distinguished Visitor program. The ATCA is part of the Australia Telescope National Facility which is funded by the Commonwealth of Australia for operation as a National Facility managed by CSIRO. This paper includes archived data obtained through the Australia Telescope Online Archive (<http://atoa.atnf.csiro.au>). The MOST is operated by the University of Sydney with support from the Australian Research Council.

REFERENCES

- Altenhoff W., Mezger P.G., Wendker H., Westerhout G., 1960, Veröff. Sternwarte Bonn, No 59, 48
 Bartel N. et al., 2000, *Science*, 287, 112
 Bauer F.E., Smartt S., Immler S., Brandt W.N., Weiler K.W., 2007, *AIP Conference Proceedings*, 937, 427
 Bauer F.E., Dwarkadas V.V., Brandt W.N., Immler S., Smartt S., Bartel N., Bietenholz M.F., 2008, *ApJ*, 688, 1210
 Berezhko E.G., Ksenofontov L.T., 2006, *ApJ*, 650, 59
 Bietenholz M.F., Bartel N., Rupen M.P., 2010, *ApJ*, 712, 1057
 Bock D.C.-J., Large M.I., Sadler E.M., 1999, *AJ*, 117, 1578
 Chandra P., Ray A., Bhatnagar S., 2004, *ApJ*, 612, 974C
 Chandra P. et al., 2009, *ApJ*, 690, 1839C
 Chevalier R.A., 1982, *ApJ*, 259, 302
 Chevalier R.A., 1996, *ASPC*, 93, 125
 Chevalier R.A., Liang E.P., 1989, *ApJ*, 344, 332
 Chevalier R.A., Fransson C., 1994, *ApJ*, 420, 268
 Dewey D., Bauer F.E., Dwarkadas V.V., 2011, *AIPC*, 1358, 289D
 Duffy P., Ball L., Kirk J.G., 1995, *ApJ*, 447, 364
 Dwarkadas V.V., 2005, *ApJ*, 630, 892
 Dwarkadas V.V., 2007a, *ApJ*, 667, 226
 Dwarkadas V.V., 2007b, *Revista Mexicana de Astronomía y Astrofísica Conference Series*, 30, 49
 Dwarkadas V.V., 2007c, *Supernova 1987A: 20 Years After: Supernovae and Gamma-Ray Bursters*, 937, 120
 Dwarkadas V.V., Dewey D., Bauer F.E., 2010, *MNRAS*, 407, 812
 Ellison D.C., Decourchelle A., Ballet J., 2004, *A&A*, 413, 189
 Elmouttie E., Haynes R.F., Jones K.L., Ehle M., Beck R., Wielebinski R., 1995, *MNRAS*, 275, L53
 Ensmann L., Burrows A., 1992, *ApJ*, 393, 742
 Fransson C., Björnsson C., 1998, *ApJ*, 509, 861
 Freeman K.C., Karlsson B., Lynga G., Burrell J.F., van Woerden H., Goss W.M., Mebold U., 1977, *A&A*, 55, 445
 Greenhill L.J., Ellingsen S.P., Norris R.P., Gough R.G., Sinclair M.W., Moran J.M., Mushotzsky R., 1997, *ApJ*, 474, L103
 Isobe T., Feigelson E.D., Akritas M., Babu G.J., 1990, *ApJ*, 364, 104
 Jones K.L., Koribalski B.S., Elmouttie M., Haynes R.F., 1999, *MNRAS*, 302, 649
 Koribalski B.S. et al., 2004, *AJ*, 128, 16
 Lamers H.J.G.L.M., Maeder A., Schmutz W., Cassinelli J.P., 1991, *ApJ*, 368, 538
 Lundqvist P., Fransson C., 1996, *ApJ*, 464, 924
 Marcaide J.M. et al., 1997, *ApJL*, 486, L31
 Martí-Vidal I., Marcaide J.M., Alberdi A., Guirado J.C., Prez-Torres M.A., Ros E., 2011, *A&A*, 526, A143
 McCallum J.N., Ellingsen S.P., Jauncey D.L., Lovell J.E.J., Greenhill L.J., 2005, *AJ*, 129, 1231
 McCallum J.N., Ellingsen S.P., Lovell J.E.J., 2007, *MNRAS*, 376, 549
 McCallum J.N., Ellingsen S.P., Lovell J.E.J., Phillips C.J., Reynolds J.E., 2009, *MNRAS*, 392, 1339
 Mioduszewski A.J., Dwarkadas V.V., Ball L., 2001, *ApJ*, 562, 869
 Montes M.J., Van Dyk S.D., Weiler K.W., Sramek R.A.,

- Panagia N., 1998, *ApJ*, 506, 874M
- Montes M.J., Weiler K.W., Van Dyk S.D., Panagia N., Lacey C.K., Sramek R.A., Park R., 2000, *ApJ*, 532, 1124M
- Nugis T., Lamers H.J.G.L.M., 2000, *A&A*, 360, 227
- Park S., Zhekov S.A., Burrows D.N., McCray R., 2005, *ApJ*, 634, L73
- Phillips C.J., Norris R.P., Ellingsen S.P., McCulloch P.M., 1998, *MNRAS*, 300, 1131
- Readhead A.C.S., 1994, *ApJ*, 426, 51
- Reynolds S.P., 2008, *ARAA*, 46, 89
- Ryder S.D., Sadler E.M., Subrahmanyan R., Weiler K.W., Panagia N., Stockdale C.J., 2004, *MNRAS*, 349, 1093
- Seager S., Sasselov D.D., Scott D., 2000, *ApJS*, 128, 407
- Smith I.A., Ryder S.D., Böttcher M., Tingay S.J., Stacy A., Pakull M., Liang E.P., 2007, *ApJ*, 669, 1130
- Soderberg A.M., Chevalier R.A., Kulkarni S.R., Frail D.A., 2006, *ApJ*, 651, 1005
- Stothers R.B., Chin C.-W., 1996, *ApJ*, 468, 842
- Tatischeff V., 2009, *A&A*, 499, 191
- Tenorio-Tagle G., Bodenheimer P., Franco J., Rozycka M., 1990, *MNRAS*, 244, 563
- Tenorio-Tagle G., Rozycka M., Franco J., Bodenheimer P., 1991, *MNRAS*, 251, 318
- Vink J.S., Muijres L.E., Anthonisse B., de Koter A., Gräfener G., Langer N., 2011, *A&A*, 531A, 132V
- Weaver R., McCray R., Castor J., Shapiro P., Moore R., 1977, *ApJ*, 218, 377
- Weiler K.W., Panagia N., Montes M.J., Sramek R.A., 2002, *ARAA*, 40, 387
- Weiler K.W., Williams C.L., Panagia N., Stockdale C.J., Kelley M.T., Sramek R.A., Van Dyk S.D., Marcaide J.M., 2007, *ApJ*, 671, 1959
- Weiler K.W., Panagia N., Stockdale C., Rupen M., Sramek R.A., Williams C.L., 2011, *ApJ*, 740, 79W
- Wilson W.E. et al., 2011, *MNRAS*, 416, 832
- Zanardo G. et al., 2010, *ApJ*, 710, 1515

6 APPENDIX

Below we provide flux density tables for the calibrators and nucleus measurements (Tables A1 and A2 respectively) which are shown in the lower panels of Fig. 1. These were reduced in the same manner as the flux densities of SN 1996cr, and demonstrate that the variability we see is real. The full tables are available in the online journal.

Table A1. Calibrators

Obs. Date	Obs. ID	Calibrator	W-Band		K _a -Band		K-Band		X-Band		C-Band		S-Band		L-Band	
			ν	S_ν	ν	S_ν	ν	S_ν	ν	S_ν	ν	S_ν	ν	S_ν	ν	S_ν
(1)	(2)	(3)	(4)	(5)	(6)	(7)	(8)	(9)	(10)	(11)	(12)	(13)	(14)	(15)	(16)	(17)
1995-03-03	C204a	1329-665	—	—	—	—	—	—	8640	348.0 \pm 11.6	4800	854.0 \pm 14.1	—	—	—	—
1995-03-03	C204a	1329-665	—	—	—	—	—	—	8640	348.0 \pm 11.6	4800	854.0 \pm 14.1	—	—	—	—
1995-03-30	C363	1329-665	—	—	—	—	—	—	—	—	—	—	—	—	1418	2680.0 \pm 34.0
1995-04-16	C418	1329-665	—	—	—	—	—	—	—	—	—	—	2378	1660.0 \pm 17.1	1418	2650.0 \pm 50.4
1995-05-27	C204a	1329-665	—	—	—	—	—	—	8640	347.0 \pm 27.7	4800	855.0 \pm 15.8	—	—	—	—
1995-05-27	C204a	1329-665	—	—	—	—	—	—	8640	347.0 \pm 27.7	4800	855.0 \pm 15.8	—	—	—	—
1995-06-07	C204a	1329-665	—	—	—	—	—	—	8640	348.0 \pm 12.9	4800	853.0 \pm 15.3	—	—	—	—
1995-06-07	C204a	1329-665	—	—	—	—	—	—	8640	348.0 \pm 12.9	4800	853.0 \pm 15.3	—	—	—	—
1995-07-27	C204c	1329-665	—	—	—	—	—	—	—	—	—	—	2368	1680.0 \pm 15.1	1376	2860.0 \pm 19.9
1995-08-03	C363	1329-665	—	—	—	—	—	—	—	—	—	—	—	—	1418	2480.0 \pm 82.3
1996-02-06	CT09	1718-649	—	—	—	—	—	—	—	—	—	—	—	—	1664	3640.0 \pm 61.4
1996-08-01	C466	1236-684	—	—	—	—	—	—	8640	355.0 \pm 15.6	4800	283.0 \pm 9.6	—	—	—	—
1996-12-05	C505	1236-684	—	—	—	—	—	—	—	—	—	—	2368	572.0 \pm 13.3	1384	747.0 \pm 15.5
1996-12-15	C586	1549-790	—	—	—	—	—	—	8512	2320.0 \pm 18.0	4928	3490.0 \pm 16.7	—	—	—	—
1996-12-15	C586	1549-790	—	—	—	—	—	—	8512	2320.0 \pm 18.0	4928	3490.0 \pm 16.7	—	—	—	—
1997-06-17	V100C	1045-62	—	—	—	—	—	—	8425	1640.0 \pm 59.8	—	—	—	—	—	—
1997-06-17	V100C	1045-62	—	—	—	—	—	—	8425	1430.0 \pm 52.7	—	—	—	—	—	—
1997-12-05	V099	1104-445	—	—	—	—	—	—	—	—	—	—	2268	2890.0 \pm 79.8	—	—
1997-12-05	V099	1104-445	—	—	—	—	—	—	—	—	—	—	2268	2610.0 \pm 32.2	—	—
1997-12-31	C694	1414-59	—	—	—	—	—	—	6024	819.0 \pm 38.5	4800	891.0 \pm 20.2	—	—	—	—
1999-06-19	C788	1329-665	—	—	—	—	—	—	—	—	—	—	—	—	1418	2600.0 \pm 71.2
1999-06-19	C788	1329-665	—	—	—	—	—	—	—	—	—	—	—	—	1384	2670.0 \pm 14.0
2000-06-19	V137	1424-418	—	—	—	—	22215	1650.0 \pm 35.7	—	—	—	—	—	—	—	—
2000-06-19	V137	1424-418	—	—	—	—	22203	1580.0 \pm 56.8	—	—	—	—	—	—	—	—
2000-06-19	V137	1424-418	—	—	—	—	22190	1590.0 \pm 35.1	—	—	—	—	—	—	—	—
2002-07-18	V137	1610-771	—	—	—	—	22224	2100.0 \pm 21.0	—	—	—	—	—	—	—	—
2002-07-18	V137	1610-771	—	—	—	—	22216	2100.0 \pm 20.4	—	—	—	—	—	—	—	—
2002-07-18	V137	1610-771	—	—	—	—	22201	2070.0 \pm 36.5	—	—	—	—	—	—	—	—
2002-07-18	V137	1610-771	—	—	—	—	22187	2100.0 \pm 11.1	—	—	—	—	—	—	—	—
2002-07-18	V137	1610-771	—	—	—	—	22172	2100.0 \pm 19.4	—	—	—	—	—	—	—	—
2003-09-07	C1224	1414-59	—	—	—	—	23659	1190.0 \pm 17.8	—	—	—	—	—	—	—	—
2003-11-03	C1049	1414-59	—	—	—	—	19008	1150.0 \pm 30.7	—	—	—	—	—	—	—	—
2003-11-03	C1049	1414-59	—	—	—	—	16960	1160.0 \pm 30.4	—	—	—	—	—	—	—	—
2003-11-04	C1049	1414-59	—	—	—	—	22796	1200.0 \pm 69.7	—	—	—	—	—	—	—	—
2003-11-04	C1049	1414-59	—	—	—	—	21056	1220.0 \pm 59.9	—	—	—	—	—	—	—	—
2003-11-08	C1049	1414-59	—	—	—	—	—	—	8256	1230.0 \pm 33.0	5056	954.0 \pm 24.1	—	—	—	—
2004-04-02	C1424	1338-58	—	—	—	—	—	—	8640	433.0 \pm 18.0	4800	918.0 \pm 14.6	2368	1880.0 \pm 27.6	1384	2800.0 \pm 35.3
2004-05-20	CX065	1414-59	—	—	—	—	22087	1100.0 \pm 50.0	—	—	—	—	—	—	—	—

Table A1 (cont'd)

Obs. Date	Obs. ID	Calibrator	W-Band		K _a -Band		K-Band		X-Band		C-Band		S-Band		L-Band	
			ν	S_ν	ν	S_ν	ν	S_ν	ν	S_ν	ν	S_ν	ν	S_ν	ν	S_ν
(1)	(2)	(3)	(4)	(5)	(6)	(7)	(8)	(9)	(10)	(11)	(12)	(13)	(14)	(15)	(16)	(17)
2004-06-13	V176	1414-59	—	—	—	—	22209	1140.0 ± 38.0	—	—	—	—	—	—	—	—
2004-06-13	V176	1414-59	—	—	—	—	22195	1150.0 ± 38.5	—	—	—	—	—	—	—	—
2004-08-01	V176B	1414-59	—	—	—	—	22209	993.0 ± 28.8	—	—	—	—	—	—	—	—
2004-08-01	V176B	1414-59	—	—	—	—	22195	993.0 ± 31.0	—	—	—	—	—	—	—	—
2005-03-14	C1368	1414-59	—	—	—	—	22193	877.0 ± 20.9	—	—	—	—	—	—	—	—
2005-04-20	C1368	1414-59	—	—	—	—	22194	85.6 ± 20.0	—	—	—	—	—	—	—	—
2005-10-27	C1049	1414-59	—	—	—	—	18752	941.0 ± 45.5	—	—	—	—	—	—	—	—
2005-10-27	C1049	1414-59	—	—	—	—	21056	898.0 ± 66.0	—	—	—	—	—	—	—	—
2005-11-13	C1049	1414-59	—	—	—	—	—	—	8640	988.0 ± 30.0	4800	966.0 ± 25.1	—	—	—	—
2006-04-29	C1049	1414-59	—	—	—	—	18752	806.0 ± 66.3	—	—	—	—	—	—	—	—
2006-04-29	C1049	1414-59	—	—	—	—	21056	804.0 ± 93.1	—	—	—	—	—	—	—	—
2006-06-08	CX114	1352-63	—	—	—	—	22193	817.0 ± 23.0	—	—	—	—	—	—	—	—
2006-06-08	CX114	1352-63	—	—	—	—	20160	866.0 ± 32.8	—	—	—	—	—	—	—	—
2006-06-21	C1049	1414-59	—	—	—	—	—	—	8640	878.0 ± 16.3	4800	879.0 ± 13.5	—	—	—	—
2006-09-14	C1341	1329-665	—	—	—	—	—	—	—	—	—	—	—	—	1384	3040.0 ± 90.4
2006-09-14	C1341	1329-665	—	—	—	—	—	—	—	—	—	—	—	—	1418	2780.0 ± 90.4
2007-03-22	VT10C3	1352-63	—	—	—	—	—	—	8425	1120.0 ± 50.0	—	—	—	—	—	—
2007-06-24	VX013A	1352-63	—	—	—	—	22316	1060.0 ± 22.1	—	—	—	—	—	—	—	—
2007-06-24	VX013A	1352-63	—	—	—	—	22348	1190.0 ± 25.5	—	—	—	—	—	—	—	—
2008-04-21	C1803	1352-63	—	—	—	—	—	—	8640	1410.0 ± 33.0	4800	1530.0 ± 32.9	2368	1440.0 ± 41.4	1384	1250.0 ± 41.7
2008-08-16	C1750	1352-63	—	—	—	—	22192	951.0 ± 25.2	—	—	—	—	—	—	—	—
2008-10-02	C184	1352-63	—	—	34496	893.0 ± 54.2	—	—	—	—	—	—	—	—	—	—
2008-10-12	C184	1352-63	—	—	—	—	—	—	8640	1410.0 ± 31.8	4786	1610.0 ± 29.0	—	—	—	—
2008-10-12	C184	1329-665	—	—	—	—	—	—	—	—	—	—	2496	1520.0 ± 59.7	1376	2550.0 ± 77.3
2008-12-22	C184	1352-63	—	—	—	—	—	—	8640	1280.0 ± 26.4	4786	1550.0 ± 30.4	2496	1400.0 ± 30.4	1376	1270.0 ± 25.4
2009-01-28	C184	1352-63	—	—	—	—	—	—	8640	1330.0 ± 28.7	4786	1510.0 ± 30.8	2496	1420.0 ± 33.1	1376	1300.0 ± 30.4
2009-02-16	C184	1352-63	—	—	—	—	—	—	8640	1210.0 ± 27.2	4786	1490.0 ± 25.4	2496	1420.0 ± 39.6	1376	1250.0 ± 41.4
2009-04-13	CX172	1352-63	—	—	—	—	—	—	8800	1350.0 ± 18.3	5500	1560.0 ± 17.3	—	—	—	—
2010-01-16	C1726	1352-63	—	—	—	—	—	—	9000	1370.0 ± 21.2	5500	1500.0 ± 14.3	—	—	—	—
2010-05-05	V253	1352-63	—	—	—	—	22000	803.0 ± 32.3	—	—	—	—	—	—	—	—
2010-05-07	V253	1352-63	—	—	—	—	—	—	8425	1240.0 ± 11.1	—	—	—	—	—	—
2011-05-09	C2479	1329-665	—	—	—	—	—	—	—	—	—	—	2100	1550.0 ± 80.0	1418	2500.0 ± 98.0
2011-05-09	C2479	1329-665	—	—	—	—	—	—	—	—	—	—	2100	1500.0 ± 20.0	1613	2510.0 ± 69.0

Note. — *Column 1:* Starting date of observation. *Column 2:* Observing program ID. *Column 3:* Calibrator. *Columns 4, 6, 8, 10, 12, 14, and 16:* Mean frequency of observed band in units of MHz. *Columns 5, 7, 9, 11, 13, 15, and 17:* Integrated flux densities in units of mJy as measured by UVFIT in MIRIAD.

Table A2. Nucleus

Obs. Date	Obs. ID	W-Band		K _a -Band		K-Band		X-Band		C-Band		S-Band		L-Band	
		ν	S_ν	ν	S_ν	ν	S_ν	ν	S_ν	ν	S_ν	ν	S_ν	ν	S_ν
(1)	(2)	(3)	(4)	(5)	(6)	(7)	(8)	(9)	(10)	(11)	(12)	(13)	(14)	(15)	(16)
1995-01-20	C363	—	—	—	—	—	—	—	—	—	—	—	—	1418	45.8 ± 2.9
1995-02-25	C363	—	—	—	—	—	—	—	—	—	—	—	—	1418	65.0 ± 3.1
1995-03-03	C204a	—	—	—	—	—	—	8640	22.7 ± 9.0	4800	44.9 ± 4.3	—	—	—	—
1995-03-03	C204a	—	—	—	—	—	—	8640	37.4 ± 9.2	4800	45.5 ± 4.4	—	—	—	—
1995-03-30	C363	—	—	—	—	—	—	—	—	—	—	—	—	1418	64.3 ± 2.3
1995-04-16	C418	—	—	—	—	—	—	—	—	—	—	2768	53.4 ± 1.0	1418	62.8 ± 1.0
1995-05-27	C204a	—	—	—	—	—	—	8640	41.1 ± 11.0	4800	48.8 ± 4.9	—	—	—	—
1995-05-27	C204a	—	—	—	—	—	—	8640	48.0 ± 12.0	4800	48.6 ± 4.9	—	—	—	—
1995-06-07	C204a	—	—	—	—	—	—	8640	48.7 ± 12.0	4800	43.2 ± 4.3	—	—	—	—
1995-06-07	C204a	—	—	—	—	—	—	8640	49.1 ± 1.2	4800	42.9 ± 4.3	—	—	—	—
1995-07-27	C204c	—	—	—	—	—	—	—	—	—	—	2368	44.5 ± 3.5	1376	65.8 ± 4.0
1995-08-03	C363	—	—	—	—	—	—	—	—	—	—	—	—	1418	52.4 ± 3.0
1996-02-06	CT09	—	—	—	—	—	—	—	—	—	—	—	—	1664	56.5 ± 1.0
1996-08-01	C466	—	—	—	—	—	—	8640	114.0 ± 20.0	4800	83.3 ± 1.7	—	—	—	—
1996-12-05	C505	—	—	—	—	—	—	—	—	—	—	2368	40.2 ± 1.0	1384	50.5 ± 1.0
1996-12-15	C586	—	—	—	—	—	—	8512	55.0 ± 5.5	4928	48.1 ± 4.8	—	—	—	—
1996-12-15	C586	—	—	—	—	—	—	8512	56.4 ± 5.6	4928	48.6 ± 4.9	—	—	—	—
1997-06-17	V100C	—	—	—	—	—	—	8425	87.7 ± 16.0	—	—	—	—	—	—
1997-06-17	V100C	—	—	—	—	—	—	8425	76.9 ± 5.0	—	—	—	—	—	—
1997-12-05	V099	—	—	—	—	—	—	—	—	—	—	2268	86.3 ± 8.0	—	—
1997-12-05	V099	—	—	—	—	—	—	—	—	—	—	2268	56.4 ± 6.0	—	—
1997-12-31	C694	—	—	—	—	—	—	6024	80.8 ± 7.0	4800	67.5 ± 4.7	—	—	—	—
1999-06-19	C788	—	—	—	—	—	—	—	—	—	—	—	—	1418	48.4 ± 4.0
1999-06-19	C788	—	—	—	—	—	—	—	—	—	—	—	—	1384	45.4 ± 4.0
2000-06-19	V137	—	—	—	—	22215	94.2 ± 8.4	—	—	—	—	—	—	—	—
2000-06-19	V137	—	—	—	—	22203	95.2 ± 7.0	—	—	—	—	—	—	—	—
2000-06-19	V137	—	—	—	—	22190	107.0 ± 7.1	—	—	—	—	—	—	—	—
2002-07-18	V137	—	—	—	—	22224	79.3 ± 10.0	—	—	—	—	—	—	—	—
2002-07-18	V137	—	—	—	—	22216	73.9 ± 8.0	—	—	—	—	—	—	—	—
2002-07-18	V137	—	—	—	—	22201	83.2 ± 8.7	—	—	—	—	—	—	—	—
2002-07-18	V137	—	—	—	—	22187	68.2 ± 8.1	—	—	—	—	—	—	—	—
2002-07-18	V137	—	—	—	—	22172	78.9 ± 9.0	—	—	—	—	—	—	—	—
2003-09-07	C1224	—	—	—	—	23659	90.0 ± 9.0	—	—	—	—	—	—	—	—
2003-11-03	C1049	—	—	—	—	19008	96.0 ± 8.0	—	—	—	—	—	—	—	—
2003-11-03	C1049	—	—	—	—	16960	97.0 ± 9.4	—	—	—	—	—	—	—	—
2003-11-04	C1049	—	—	—	—	22796	109.0 ± 11.0	—	—	—	—	—	—	—	—
2003-11-04	C1049	—	—	—	—	21056	107.0 ± 10.0	—	—	—	—	—	—	—	—
2003-11-08	C1049	—	—	—	—	—	—	8256	98.2 ± 6.3	5056	78.0 ± 8.5	—	—	—	—

Table A2 (cont'd)

Obs. Date	Obs. ID	W-Band		K _a -Band		K-Band		X-Band		C-Band		S-Band		L-Band	
		ν	S_ν	ν	S_ν	ν	S_ν	ν	S_ν	ν	S_ν	ν	S_ν	ν	S_ν
(1)	(2)	(3)	(4)	(5)	(6)	(7)	(8)	(9)	(10)	(11)	(12)	(13)	(14)	(15)	(16)
2004-04-02	C1424	—	—	—	—	—	—	8640	78.9 ± 7.2	4800	71.4 ± 4.7	2368	52.0 ± 2.2	1384	52.2 ± 2.0
2004-05-20	CX065	—	—	—	—	22087	108.0 ± 9.9	—	—	—	—	—	—	—	—
2004-06-13	V176	—	—	—	—	22209	71.7 ± 1.2	—	—	—	—	—	—	—	—
2004-06-13	V176	—	—	—	—	22195	67.1 ± 1.1	—	—	—	—	—	—	—	—
2004-08-01	V176B	—	—	—	—	22209	77.7 ± 9.5	—	—	—	—	—	—	—	—
2004-08-01	V176B	—	—	—	—	22195	76.5 ± 9.5	—	—	—	—	—	—	—	—
2005-03-14	C1368	—	—	—	—	22193	446.0 ± 17.0	—	—	—	—	—	—	—	—
2005-04-20	C1368	—	—	—	—	22194	454.0 ± 20.0	—	—	—	—	—	—	—	—
2005-05-25	C1321	88632	40.0 ± 7.0	—	—	—	—	—	—	—	—	—	—	—	—
2005-10-27	C1049	—	—	—	—	18752	87.7 ± 9.3	—	—	—	—	—	—	—	—
2005-10-27	C1049	—	—	—	—	21056	80.6 ± 9.8	—	—	—	—	—	—	—	—
2005-11-13	C1049	—	—	—	—	—	—	8640	60.7 ± 3.8	4800	79.7 ± 2.0	—	—	—	—
2006-04-29	C1049	—	—	—	—	18752	99.6 ± 1.1	—	—	—	—	—	—	—	—
2006-04-29	C1049	—	—	—	—	21056	88.7 ± 9.4	—	—	—	—	—	—	—	—
2006-06-08	CX114	—	—	—	—	22193	448.0 ± 23.9	—	—	—	—	—	—	—	—
2006-06-08	CX114	—	—	—	—	20160	57.0 ± 15.0	—	—	—	—	—	—	—	—
2006-06-21	C1049	—	—	—	—	—	—	8640	67.3 ± 1.1	4800	84.6 ± 1.0	—	—	—	—
2006-09-14	C1341	—	—	—	—	—	—	—	—	—	—	—	—	1384	35.0 ± 9.2
2006-09-14	C1341	—	—	—	—	—	—	—	—	—	—	—	—	1418	56.5 ± 5.8
2007-06-24	VX013A	—	—	—	—	22316	138.0 ± 7.5	—	—	—	—	—	—	—	—
2007-06-24	VX013A	—	—	—	—	22348	147.0 ± 7.2	—	—	—	—	—	—	—	—
2008-04-21	C1803	—	—	—	—	—	—	8640	56.1 ± 2.8	4800	65.4 ± 5.8	2368	57.4 ± 5.3	1384	64.0 ± 5.2
2008-08-16	C1750	—	—	—	—	22192	241.0 ± 14.6	—	—	—	—	—	—	—	—
2008-10-02	C184	—	—	34496	78.1 ± 8.2	—	—	—	—	—	—	—	—	—	—
2008-10-12	C184	—	—	—	—	—	—	8640	54.0 ± 5.5	4786	52.2 ± 6.8	—	—	—	—
2008-10-12	C184	—	—	—	—	—	—	—	—	—	—	2496	128.0 ± 34.3	1376	122.0 ± 32.0
2008-12-22	C184	—	—	—	—	—	—	8640	46.0 ± 8.3	4786	74.0 ± 9.0	2496	120.0 ± 31.7	1376	83.1 ± 13.2
2009-01-28	C184	—	—	—	—	—	—	8640	60.6 ± 7.3	4786	74.0 ± 8.4	2496	71.9 ± 14.3	1376	82.4 ± 2.2
2009-04-13	CX172	—	—	—	—	—	—	8800	49.8 ± 5.2	5500	41.0 ± 5.1	—	—	—	—
2010-01-16	C1726	—	—	—	—	—	—	9000	68.2 ± 5.4	5500	74.8 ± 6.7	—	—	—	—
2010-01-25	C184	—	—	—	—	—	—	—	—	—	—	2450	62.8 ± 1.0	—	—
2010-05-05	V253	—	—	—	—	22316	51.0 ± 4.9	—	—	—	—	—	—	—	—
2010-05-07	V253	—	—	—	—	—	—	8425	90.6 ± 7.0	—	—	—	—	—	—
2011-05-09	1.5B	—	—	—	—	—	—	—	—	—	—	2100	63.0 ± 6.5	1418	76.3 ± 5.2
2011-05-09	1.5B	—	—	—	—	—	—	—	—	—	—	2100	65.0 ± 6.3	1613	90.6 ± 20.4

Note. — Column 1: Starting date of observation. Column 2: Observing program ID. Columns 3, 5, 7, 9, 11, 13, and 15: Mean frequency of observed band in units of MHz. Columns 4, 6, 7, 10, 12, 14, and 16: Integrated flux densities in units of mJy as measured by UVFIT or IMFIT in MIRIAD.